Small

NANO · MICRO small
www.small-journal.com

RESEARCH ARTICLE

Unveiling Copper Vanadium Sulfide Nanocrystals as a Next-Generation Electrocatalyst for Selective Nitrate Remediation to Ammonia

Smruti Sourav[1] | Jit Satra[2] | Ram Sewak[3] | Ujjwala. P. Thayyil[1] | Shovon Chatterjee[1] | Surajit Mondal[1] | Anirban Mondal[3] | Nimai Mishra[1]

[1]Department of Chemistry Institute of Chemical Technology Mumbai, Indian Oil Odisha Campus Bhubaneswar, IIT Kharagpur Extension Center, Samantipuri Mouza, Bhubaneswar, Odisha, India | [2]Department of Chemistry Institute of Science, Banaras Hindu University, Varanasi, UP, India | [3]Department of Chemistry, Indian Institute of Technology Gandhinagar, Gandhinagar, Gujarat, India

Correspondence: Nimai Mishra (n.mishra@iocb.ictmumbai.edu.in)

Received: 16 October 2025 | **Revised:** 1 January 2026 | **Accepted:** 2 January 2026

Keywords: ammonia synthesis | Cu_3VS_4 nanocrystals | electrocatalysis | nitrate reduction reaction (NORR) | ternary chalcogenides

ABSTRACT

The Haber-Bosch process dominates ammonia production but is energy-intensive and a major source of COx emissions. Electrochemical nitrate reduction (NORR) presents a sustainable alternative by simultaneously remediating nitrate pollution and enabling carbon-neutral, or even carbon-negative, ammonia synthesis. However, NORR still suffers from high overpotentials, limited selectivity, and poor catalyst durability. Here, a one-pot hydrothermal strategy is reported for synthesizing ternary copper-vanadium sulfide (CVS) nanocrystals as a robust, heavy-metal-free NORR electrocatalyst operating under ambient conditions. The synergistic Cu-V interactions within the sulvanite framework enhance reduction activity, while vertical stacking and high crystallinity provide a large electrochemically active surface area and efficient charge transport. CVS delivers a significantly low onset potential (−0.476 V) and overpotential (−0.596 V at 10 mA cm^{-2} vs RHE), rapid kinetics (Tafel slope: 34.1 mV dec^{-1}), and a high Faradaic efficiency (FE) of 91%, outperforming binary counterparts such as VS_2 and CuS. Importantly, its potential efficacy is validated using real agricultural runoff water, demonstrating practical relevance beyond laboratory conditions. Further, detailed computational studies including catalytic free energy calculations on the CVS (110) surface reveal favorable reaction energetics, consistent with experimental observations. Overall, this unique work positions ternary chalcogenides as promising platforms for decentralized and sustainable green ammonia synthesis.

1 | Introduction

Ammonia is a versatile compound with diverse applications across agriculture [1], pharmaceuticals [2], energy production [3], industrial processes [4], textile industry [5], and food technology [6] and so on. It's exceptionally low boiling point [7] makes it indispensable in cryogenics, where extreme cooling is essential. Rich in hydrogen content, ammonia emerges as a promising energy-dense fuel [8], which can be transported easily compared to hydrogen, aligning with the global shift toward sustainable energy solutions. Excitingly, it has recently captured attention as a potential propellant in space exploration [9], offering a carbon-free alternative for advancing the frontiers of science and technology.

Smruti Sourav and Jit Satra contributed equally to this work.

Since the development to meet the ammonia demand during World War I, the Haber-Bosch process has been extensively employed for the large-scale thermocatalytic synthesis of ammonia [10]. This energy-intensive method, invented by German chemists Fritz Haber and Carl Bosch in 1909, remains fundamental in industrial ammonia production to date. The thermo-catalytic reaction between hydrogen and nitrogen for ammonia production, given below, requires high temperature and high pressure to break the strong triple bond of molecular nitrogen gas.

$$N_2\,(g) + 3H_2\,(g) \rightarrow 2NH_3\,(g) \quad \Delta H = -92kJMol^{-1}$$

While this method ensures high ammonia yields, it is accompanied by significant greenhouse gas emissions, which are approximately 1.6 tonnes of carbon dioxide for every tonne of ammonia produced [11], posing serious environmental concerns. To address this, many efforts are directed toward developing sustainable alternatives [12, 13], including utilizing renewable energy sources [14] and electrochemical methods [15, 16], to achieve efficient as well as eco-friendly ammonia synthesis. In this context, electrocatalytic ammonia production in aqueous systems has gained significant research interest due to its ability to operate under ambient conditions [17, 18], achieve zero contaminant emissions, and utilize renewable energy as a driving force, leaving behind carbon carbon-neutral/negative energy solution. This method offers a flexible production scale, making it well-suited for integration with intermittent renewable sources like solar and wind energy. Researchers initially utilized atmospheric nitrogen as the source for nitrogen reduction reaction (NRR) but there are some drawbacks for this catalytic process as follows: i) the high dissociation energy of the N≡N bond (~941 kJ mol^{-1}) ii) low solubility of nitrogen in water (0.66 mmol L^{-1}), making this unfavorable for efficient reaction kinetics. Therefore, to address these issues, the scientific community has redirected its attention toward the nitrate reduction reaction (NORR) *via* a low-energy barrier solid-liquid interface pathway [19–21], compared to the NRR where the solubility of nitrate in water (>2 mol L^{-1}) is way higher, at the same time the dissociation energy of the N═O bond (~240 kJ mol^{-1}) is considerably lower making NORR a more feasible alternative.

Moreover, since nitrate has been a key ingredient in agricultural fertilizers [22], manures [23], strengthening agents in glass and ceramic industries [24], industrial explosives [25], and military applications [26], also poses significant health and environmental risks due to its high toxicity as well as excessive nitrate levels can lead to hazardous diseases [27, 28] and ecological damage, highlighting the urgent need not only for effective remediation strategies but also for their conversion into value-added products like ammonia.

Electrocatalytic NORR involves proton coupled electron transfer (PCET) process, which includes 8-electron/9-proton transport with multiple intermediates [29], where higher negative potentials boost NH_3 yield but also promote competing Hydrogen Evolution Reaction (HER) and other byproducts [30]. Thus, designing catalysts that selectively reduce nitrate to NH_3 while suppressing HER and side products is crucial.

In this regard, nanocrystals with distinctive electronic architecture emerge as highly promising electrocatalysts due to their supporting electronic environment as well as large surface area, which provides abundant active sites, resulting in high intrinsic conductivity [31–33], making them ideal for efficient NORR. Particularly for NORR, among metal-based electrocatalysts, noble metals like platinum, gold, and palladium suffer from low Faradaic Efficiency (FE) as well as utility, due to competing superior HER [34] and their high cost. In contrast, low-cost copper is particularly effective due to its exceptional physicochemical properties beneficial for durable electrocatalytic NORR while suppressing HER [35–37]. However, copper-only based nanocrystals suffer from poor activity and limited stability due to leaching issues and weak binding with nitrate intermediates, which hinder sustained NORR performance [38]. Recent research has addressed this challenge by incorporating Cu into other nanoscale materials, which improves catalytic activity and stability by bringing some unique synergistic interactions. Strikingly, vanadium steals the spotlight as its vacant d orbitals promote strong electrostatic interactions with NO_3^- oxygen atoms, optimizing the d-band center for better overlap with the nitrate's LUMO π^* orbitals, which promotes superior nitrate adsorption, activation [39–41], while its flexible oxidation states (+2 to +5) drive multistep redox reactions, making it the key player in enhancing NORR performance. This flexibility helps in driving a complex multi-electron transfer process required for complete nitrate reduction to ammonia. Nowadays, researchers have become interested in metal sulfide nanocrystals as promising electrocatalysts for crucial energy and environmental applications due to their tunable electronic bandgaps, well-positioned energy levels, and rich surface-active sites. Unlike rigid metal oxides, metal sulfides can accommodate volume changes during electrocatalysis, especially layered architectures (VS_2, MoS_2 and WS_2) with abundant edge sites that provide high catalytic activity, large surface area, and excellent stability under harsh conditions [42, 43]. Beyond these layered forms, sulfide nanocrystals offer further advantages, as their well-defined crystalline domains and controlled size distribution expose a higher density of edge and corner sites, which are typically more catalytically active than basal planes, making them particularly attractive for efficient electrocatalysis. Therefore, metal chalcogenide-based catalysts enhance NORR performance by creating abundant active sites, facilitating charge transfer through tunable bandgaps, and leveraging metal–metal synergy to optimize electronic structure for efficient nitrate adsorption, activation, and multi-electron transfer toward ammonia [39–41].

Herein, we report a one-pot hydrothermal synthesis of sulvanite-type Cu_3VS_4 (CVS) nanocrystals, designed with cost-effective and environmentally benign Cu-V synergy as a next-generation NORR electrocatalyst. The sulvanite lattice, featuring open channels and vertically stacked nanoarchitecture, facilitates rapid ion diffusion, efficient charge transport, and reduced Warburg resistance, directly translating to accelerated reaction kinetics. Compared with binary analogues (VS_2, CuS), CVS achieves a lower onset potential (−0.476 V), smaller overpotential (η_{10} = −0.596 V), and the lowest Tafel slope (34.1 mV·dec^{-1}), underscoring its superior charge-transfer kinetics. Electrochemical impedance measurements confirm minimized resistance, while the optimized conduction band alignment ensures selective nitrate activation over competing HER. Importantly, unique gas

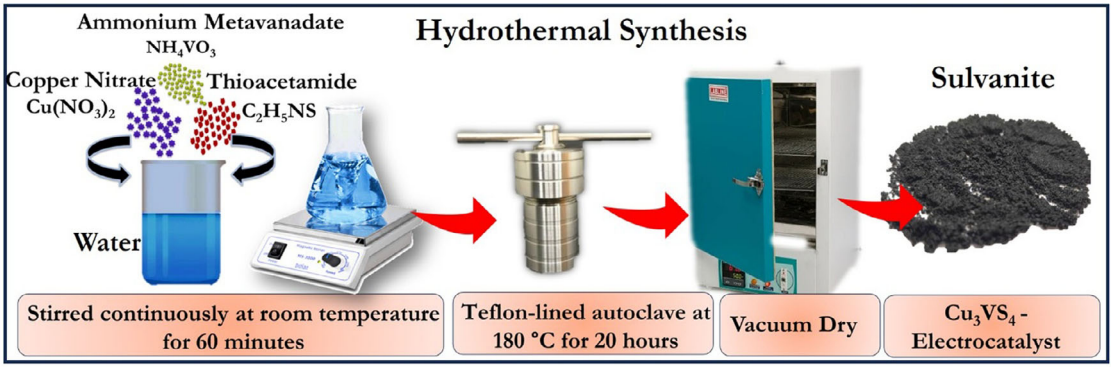

SCHEME 1 | Schematic of the synthesis procedure of the ternary chalcogenide (CVS).

chromatography measurements allowed unambiguous differentiation of HER and NORR potentials, providing rare mechanistic clarity in nitrate electroreduction systems. Chronoamperometry(CA) at −1.3 V versus RHE delivers a high FE of 91.2% for NH_3 with robust stability across 50 cycles. Complementary DFT calculations identify NO_3^- adsorption on V sites as the rate-determining step, corroborating experimental insights into the Cu-V synergistic pathway. Finally, practical validation using agricultural runoff achieved ~59% nitrate conversion, demonstrating the technological viability of CVS under realistic conditions. Collectively, the structural, electronic, and mechanistic features establish CVS as a stable, selective, and high-performance catalyst for ambient electrochemical nitrate-to-ammonia conversion for sustainable energy solutions.

2 | Results and Discussion

The materials required, as well as all the detailed experimental procedures regarding synthesis and characterization, can be found in Sections S1–S5. Ternary chalcogenide Cu_3VS_4 (CVS) was successfully synthesized via a bottom-up hydrothermal method. In brief, accurately weighed amounts of the precursor salts of NH_4VO_3, $Cu(NO_3)_2$, and C_2H_5NS were homogeneously stirred in double-distilled water at room temperature for 60 min. The resulting mixture was then transferred into a Teflon-lined stainless-steel autoclave, which was sealed and placed in a hydrothermal reactor at 180°C for 20 h. After naturally cooling to room temperature, the product was collected, washed thoroughly with ethanol several times, and vacuum-dried for subsequent physical and chemical characterization. The schematic representation of the synthesis process is illustrated in Scheme 1. For comparison, binary chalcogenides containing vanadium and copper, such as VS_2 and CuS, were also synthesized under identical hydrothermal conditions.

First, to verify the phase purity and crystallographic structure of the as-prepared targeted materials, VS_2, CuS, and CVS, Powder X-ray diffraction (PXRD) analysis was performed. The sharp diffraction peaks of CVS (Figure 1a) closely align with the standard cubic pattern of sulvanite crystal structure with Joint Committee on Powder Diffraction Standards (JCPDS) number 01-088-1318, showing prominent reflections corresponding to the (100), (110), (111), (200), (210) and (220) planes, indicating minimal presence of impurity phases. The corresponding unit cell structure of the CVS is depicted in Figure S1. The PXRD patterns for VS_2 and CuS are shown in Figure S2a,b. For VS_2, the characteristic peaks are well matched with the standard pattern for hexagonal 2H-VS_2 (JCPDS No. 01-089-1640), which are observed at 15.15°, 35.31°, and 45.11°, corresponding to the (001), (011), and (012) crystal planes, respectively. Notably, the intense and sharp (011) peak suggests a dominant formation of the 2H-phase VS_2 with excellent crystallinity. However, the presence of little residual VOOH implies that further optimization of the hydrothermal synthesis conditions is necessary to enhance phase purity. Besides this, the PXRD pattern of CuS was also verified and matched with the reference JCPDS card no. 06–0464 with distinct peaks corresponding to the (103), (006), (110), and (102) planes, confirming the formation of hexagonal-phase CuS.

To get a clear idea about the possible band energy structure in evaluating the electronic aspect of redox behavior for NORR by the catalysts, the electronic spectroscopy and Mott-Schottky (M-S) analysis were integrated [Figure 1b,c; Figure S3a,b]. From Tauc's plot, the obtained bandgap values of all the materials were found to be 1.89 eV for CVS, 2.02 eV for VS_2 and 1.68 eV for CuS. Following that, the electrochemical M-S analysis was performed, which is the change in the space-charge capacitance at the electrode/electrolyte interface *w.r.t.* the applied potential. The intercept on the X-axis represents the flat band potential (E_{fb}), which is a measure of a potential that needs to be applied for crossing the depletion layer arising from a semiconducting junction, like the interface between the electrode and the double layer formed at the electrolyte side. As the electrode-electrolyte interface is correlated to the semiconductor junction, this plot generally not only indicates the typical semiconducting nature of the material but also suggests the potential position of the Fermi level, represented by the flat band (fb) value [44]. Conventionally, a positive slope of M-S signifies the n-type, and a negative slope originates from the p-type. The M-S plots revealed that VS_2 (Figure S3c) and CVS [Figure 1c] exhibit n-type characteristics with positive slopes, while CuS displays a negative slope, confirming its p-type semiconductor nature (Figure S3d). The (E_{fb}) provided estimates of the conduction band minima (CBM) for CVS and VS_2, and it is estimated to be: −0.62 V for CVS, −0.30 V for VS_2, while +0.197 V versus RHE is the valence band maxima (VBM) for CuS, which gives rise to CBM of −1.48 V versus RHE when adding the bandgap value (Figure 1d; Figure S4). Comparing these energy levels with the standard redox potential for nitrate-to-ammonia conversion (−0.38 V vs RHE),

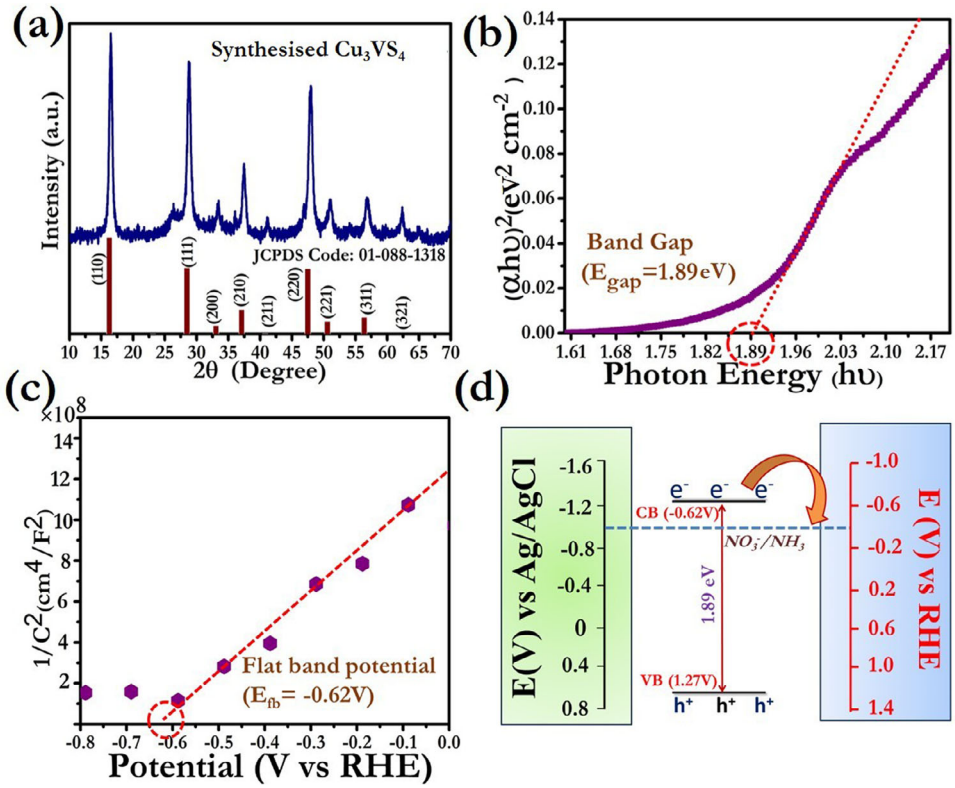

FIGURE 1 | (a) Powder XRD patterns (b) Tauc plot (c) Mott-Schottky analysis (d) Probable band energy diagram of CVS, correlating redox potential for catalysis.

it is evident that the conduction band minima CBM of VS_2 lie below or very close to this potential, offering significantly insufficient driving force to promote the reduction reaction. For CuS, the CBM is located at a highly negative potential (−1.48 V vs RHE), which provides strong electron availability but also risks accelerating the competing HER. By contrast, CVS possesses an ideally positioned CBM at −0.62 V versus RHE, which not only exceeds the thermodynamic requirement for nitrate reduction but also balances the driving force without overly favoring HER. Taken together, these results indicate that while VS_2 and CuS individually have limitations, either too weak or too strong a driving force, CVS offers the most suitable band alignment for selectively driving the nitrate-to-ammonia conversion, making it the most promising candidate for efficient catalysis in this system.

The surface morphology of the as-synthesized catalyst was thoroughly characterized using advanced microscopic techniques such as Field Emission Scanning Electron Microscopy (FESEM) and TEM. The FESEM reveals a prominent vertical alignment and dense sheet-like stacking of NCs forming a highly porous and layered architecture, as shown in Figure 2a–c. This morphological configuration can effectively augment the electrochemically active surface area (ECSA) and accessibility of catalytically active sites. The stacked architecture can also contribute to continuous conductive pathways, reducing the spatial distance for charge transfer from the catalytic sites to the underlying conductive substrate. This can minimize the number of hopping or tunnelling steps required for electrons, thereby promoting rapid electron transfer kinetics and enhancing nitrate ion diffusion at the catalyst-electrolyte interface. On the other hand, the TEM images show the uniformity in the size of the synthesized NCs (Figure 2d,e) with an average size distribution of 17 ± 3.5 nm, as shown in the size distribution histogram (Figure S5). High-resolution transmission electron microscopy (HRTEM) images of the CVS NCs reveal well-defined lattice fringes of 3.89Å (Figure 2f) corresponding to the PXRD's (110) plane, with the $P4^-3m$ space group. The TEM images of the VS_2 and CuS are depicted in Figure S6a–f, which confirm the sheet-like structure, and the fringe patterns with distinct d-spacing values can be correlated with the corresponding PXRD results.

While PXRD and microscopic investigations confirm the crystallinity and morphology of the materials, X-ray Photoelectron Spectroscopy (XPS) digs into the surface composition and oxidation states essential for evaluating electrocatalytic performance. The XPS survey spectrum of CVS (Figure 3a) confirms the presence of Cu, V, and S with binding energies consistent with Cu^+ (Cu 2p at ~930–955 eV), V^{5+} (V 2p at ~515–525 eV), and S^{2-} (S 2p at ~162–165 eV). The XPS spectra are calibrated against the C 1s peak at ~284 eV. The spectrum aligns with the expected composition of CVS, with minimal evidence of bulk oxidation. The XPS plot shows the Cu 2p region of CVS (Figure 3b). The main peaks around 932.5 eV (Cu 2p3/2) and 952.5 eV (Cu 2p1/2), along with the absence of satellite peaks, confirm the presence of Cu^+ in the material, consistent with the expected chemical environment in CVS. The absence of Cu^{2+} features supports the phase purity of the targeted compound [45]. The presence of Cu^+ is crucial in CVS because it donates electrons, tunes the vanadium active site electronically, stabilizes intermediates, and enhances the selectivity and efficiency of nitrate-to-ammonia conversion. The V 2p region for CVS (Figure 3c) reveals the presence of vanadium in the +5-oxidation state, as indicated by

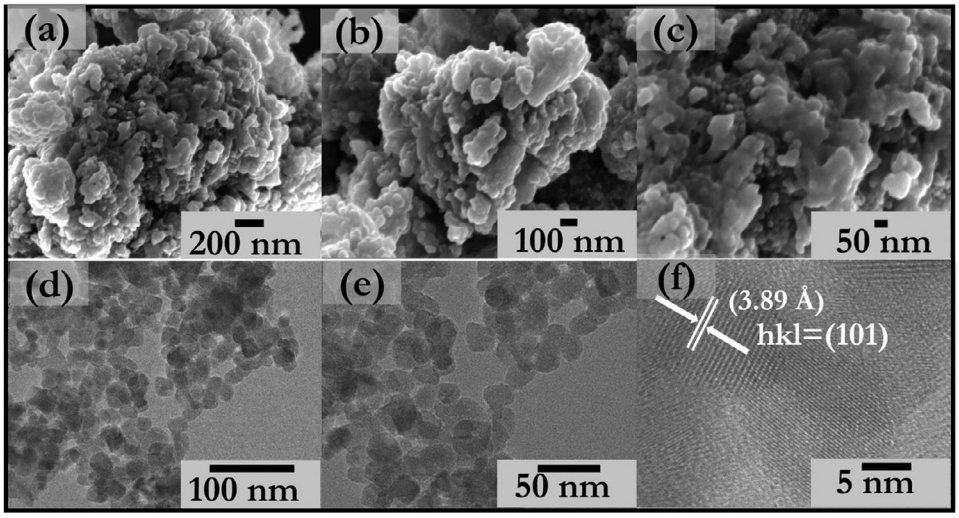

FIGURE 2 | (a–c) FESEM images showing the surface morphology and microstructural features of the synthesized catalyst at different magnifications. (d–f) Transmission electron microscopy (TEM) images revealing the internal structure and lattice fringes highlighting its nanoscale sheet architecture.

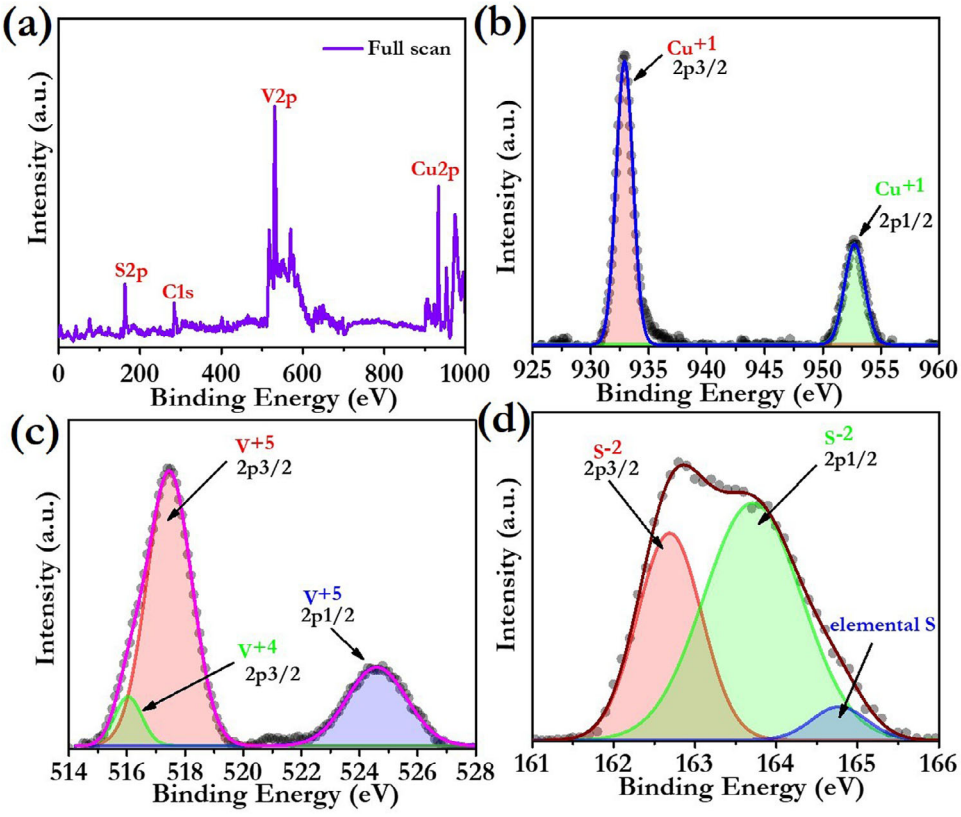

FIGURE 3 | XPS plots for CVS (a) Full Scan (b) Cu, (c) V, and (d) S.

peaks around 517.2 eV (V 2p3/2) and 524.7 eV (V 2p1/2) [45]. The trace amount of V^{4+} is shown in the graph indicating VO_2 or VS_2 which io incomparable *w.r.t* the V^{5+}. This high oxidation state of vanadium is significant because it enhances the electrophilicity of the V center, making it highly favorable for NO_3^- adsorption through electrostatic interactions and making it facile for the following multistep redox reactions to happen. Thus, the XPS directly indicates the crucial electronic contribution of vanadium in nitrate capture and conversion applications. The XPS spectrum of the S 2p region for CVS (Figure 3d) shows primarily sulfide (S^{2-}) ions at 162.56 eV (S 2p3/2) and 163.81 (S 2p1/2), confirming the material's sulfide nature, with a small amount of elemental sulfur at ~164.74 eV, likely from surface oxidation or synthesis impurities [45]. This result confirms varied sulfur environments due to Cu and V coordination in the sulvanite structure.

The XPS spectrum of Cu in CuS (Figure S7a) shows two major peaks at 933.5 eV (Cu $2p_{3/2}$) and 953.5 eV (Cu $2p_{1/2}$) with a distinct satellite peak appearing near 943 eV [46]. These satellites confirm the presence of Cu^{2+} in the CuS sample. The S 2p XPS spectrum of CuS (Figure S7b) shows peaks at around 161.7 eV (S $2p_{3/2}$) and 163.0 eV (S $2p_{1/2}$), indicating the presence of S^{2-}. In comparison, CVS typically shows S 2p peaks slightly shifted to higher binding energies (162.0-1-63.5 eV) due to the influence of V—S bonding. This shift suggests a more complex or ionic environment for sulfur in CVS compared to the more covalent Cu-S interaction in CuS. The XPS spectrum of V (Figure S7c) in VS_2 shows V 2p peaks at 516.6 and 523.9 eV, confirming the presence of V^{4+} in VS_2 [47]. There are two minor peaks of V^{3+} that appear in the spectrum, indicating a little impurity. Compared to CVS, where V^{5+} appears at higher binding energies (517.5 and 524.8 eV), this shift reflects the difference in oxidation state and local bonding environment between the two materials. The S 2p XPS peaks (Figure S7d) in VS_2 appear at 161.8 and 163.0 eV, confirming the presence of S^{2-} [47]. Compared to CVS, where S 2p peaks are slightly shifted to higher binding energies (162.0–163.5 eV), this reflects a simpler and more covalent V-S environment in VS_2 versus the mixed Cu—S and V—S bonding in CVS.

Initially, to evaluate the electrocatalytic performance toward NORR of the as-synthesized catalysts, linear sweep voltammetry (LSV) responses were recorded in 0.1 M K_2SO_4 electrolyte (pH 7) with and without the addition of 0.5 M KNO_3. The conversion of potential from Ag/AgCl to RHE is done by the Equation S1. Figure 4a shows the LSV profile of CVS, which exhibits a significant enhancement in cathodic current density upon the introduction of KNO_3, suggesting its superior electrocatalytic activity toward nitrate-assisted electrochemical processes. In contrast, the LSV profile of VS_2 in Figure 4b reveals that VS_2 shows significantly low deviation in current response upon nitrate addition, indicating either a limited interaction with nitrate species or an inherently slower charge transfer process that is not nitrate-sensitive. Whereas, the LSV for CuS catalyst, shown in Figure 4c, displays moderate enhancement in activity in the presence of nitrate, implying a partial promotion effect, though not as pronounced as observed with CVS. These differences underscore the varied nature of electron transfer kinetics and surface-nitrate interactions across the materials. A comparative analysis of the onset potential and overpotential from the standard reduction potential (i.e., at −0.42 V) at a current density of 10 mA cm^{-2} (η_{10}) is presented as a bar diagram in Figure 4d. CVS exhibits the onset potential of −0.476 V and η_{10} of −0.596 V, affirming its energetically favorable catalytic behavior. By contrast, VS_2 shows the highest onset potentials (−0.567 V) and a higher overpotential at η_{10} (−0.896 V), indicating sluggish reaction kinetics. In comparison, CuS requires the lowest onset of −0.425 V but the moderate η_{10} of −0.651 V, reinforcing its relatively inferior performance with respect to CVS. Tafel plots in Figure 4e further validate the kinetic trends, where CVS demonstrates the lowest Tafel slope of 34.1 mV dec^{-1}, indicative of rapid charge transfer and efficient electrocatalytic kinetics. On the other hand, the VS_2 and CuS display Tafel slopes of 38.4 and 46.5 mV dec^{-1}, respectively, suggesting progressively slower reaction kinetics. These findings are graphically summarized in the bar plot in Figure 4f, which concisely presents the kinetic advantage of CVS over the configurational components. Taken together, it establishes CVS as the most effective catalyst among the three, exhibiting excellent nitrate-sensitive electrocatalytic activity, lower energetic barriers, and faster electron transfer kinetics. This suggests a potentially favorable composition that facilitates enhanced adsorption and reduction of nitrate species, meriting further mechanistic investigation. In contrast, the marginal improvement with VS_2 and the limited activity of CuS highlight the importance of rational material design and surface engineering for optimized nitrate-assisted electrocatalytic green ammonia generation.

To get a mechanistic idea about the reaction kinetics of the NORR, LSV was further conducted using a Rotating Ring-Disk Electrode (RRDE) setup (Figure 5a). The NORR is a complex process involving the transfer of 8 electrons and 9 protons. This reaction encompasses two concurrent steps: (i) the diffusion of nitrate ions to the catalyst's active surface and (ii) the charge transfer from the catalyst to the nitrate at the interface between the electrolyte and the electrode. The fundamental benefit of the RRDE setup is its ability to simultaneously and quantitatively analyze reaction intermediates and products under precisely controlled mass transport conditions. The whole setup is a combination of a rotating disk (for primary reaction) with a ring electrode (for intermediate detection), where a fixed potential is maintained to oxidize the reaction product generated at the disk. Therefore, this setup enables real-time mechanistic insight that static electrodes cannot provide, which makes this invaluable for distinguishing reaction pathways and accurately evaluating catalyst performance. The CVS fabricated disk electrode surface was employed to perform LSV, varying the rotation rate from 0 to 2000 rpm at a scan rate of 50 mV s^{-1}. The disk LSV curves and the corresponding ring currents recorded at various rotation speeds are displayed in Figure 5b and Figure S8. During the nitrate-to-ammonia reduction reaction, ammonia oxidation to NO_x species also occurs at the platinum ring electrode. To validate this oxidation, the ring current was measured with the disk potential simultaneously, and subsequently a cyclic voltammetry (CV) scan was conducted at 10 mV s^{-1}, where an ammonia oxidation peak was clearly observed between 0.6 and 1.1 V versus. RHE (Figure 5c) [48]. However, it is worth noting that as the rotation speed increases, NO_x formation decreases due to a facile proton-coupled electron transfer (PCET) process that favors ammonia production. Moreover, the Koutecký-Levich (K-L) plots, obtained by linear fitting of the reciprocal current density against the reciprocal square root of the rotation rate, are presented in Figure S9. From the K-L equation, the number of electrons transferred in the diffusion-limited region was calculated to be approximately 2.3 at −0.50 V (NOx formation) and about 5.9 at −1.00 V versus RHE (NH_3 formation). These deep insights confirm that the overall process predominantly follows an eight-electron transfer pathway through NOx formation.

Based on these physicochemical insights, CA measurements were employed at different applied potentials (Figure S10) to assess the FE and NH_3 production of the developed catalyst, determining −1.3 V as the ideal potential for maximizing both activity and stability (Figure S11). To evaluate its long-term stability, CA measurements were performed, during which the catalyst demonstrated excellent stability, maintaining a current density over a period of 3 h. Furthermore, to evaluate the catalyst's recyclability, CA was carried out consecutively up to the 50th cycle at −1.3 V (Figure 6a), which shows the catalytic

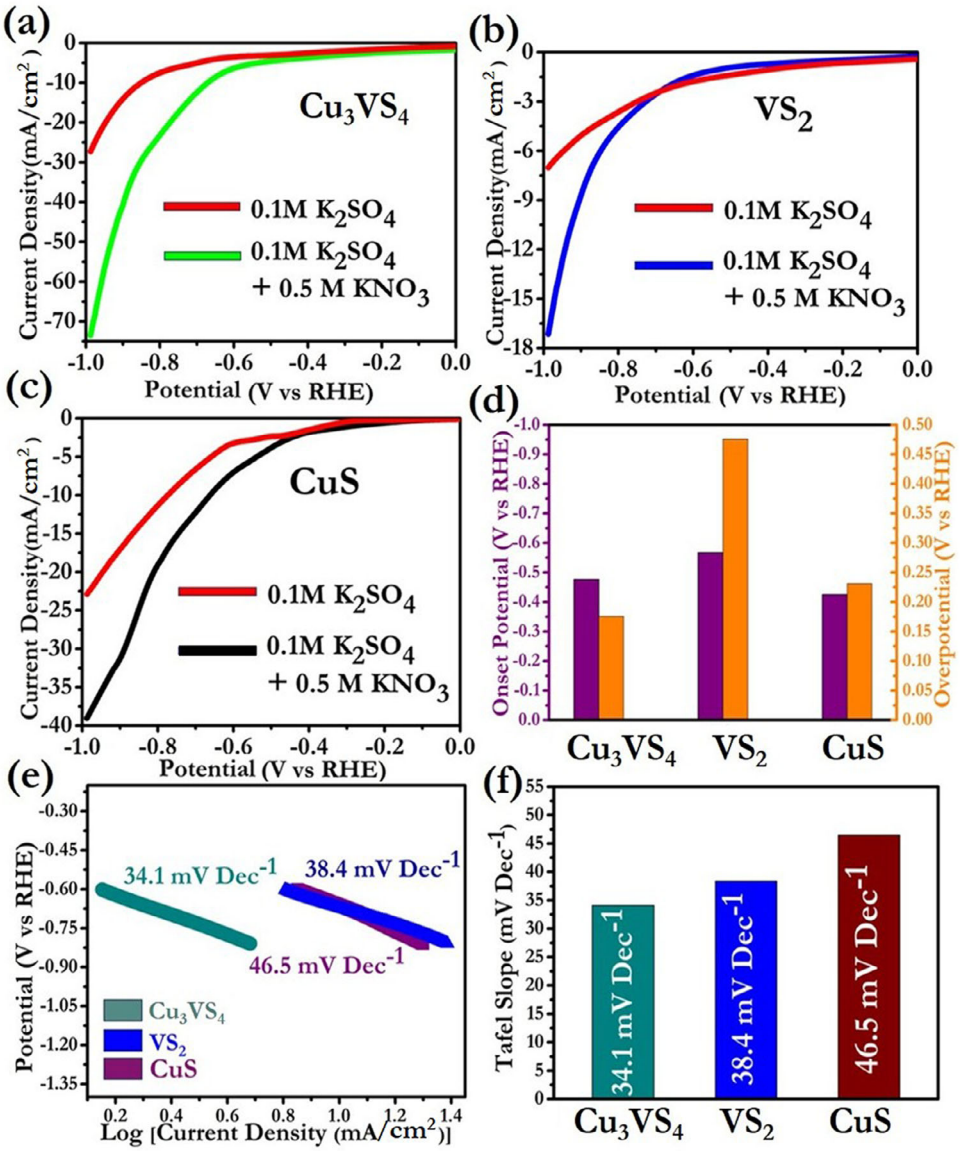

FIGURE 4 | LSV Polarization curves on changing electrolytes for (a) CVS (b) VS_2 (c) CuS, (d) Onset and overpotential bar diagram, (e) Tafel slopes (f) Corresponding bar diagram.

activity is significantly recyclable in nature. Initially in CA at −1.3 V, the current density starts at −155 mA cm^{-2} and gradually stabilizes, indicating a steady-state electrocatalytic reaction after the activation of the material in the electrolyte medium. The FE and ammonia yield were calculated by using the formulae given in (Section S4 Equations S3 and S4). The FE, presented as a bar chart (Figure 6b), starts at over 91% in the first cycle and gradually falls below 30% after whopping 50th cycle. This slow decline indicates steady selective conversion of nitrate to ammonia, with an increasing proportion of the current being slightly diverted to side reactions such as HER. The bar graph shown in Figure S12 illustrates the ammonia yield over 50 consecutive cycles which was estimated to be approximately 79 000 μg h^{-1} mg^{-1} of catalyst during the first cycle, gradually decreased to around 50 000 μg h^{-1} mg^{-1} of catalyst by the 50th cycle. It is to be mentioned that even after the 50th cycle, the current density and FE decrease by only 30% from the initial scan (Figure 6b). This trend suggests that the as-designed electrocatalyst can be employed to an industrial level for long-term electrocatalytic performance. The ^{1}H-NMR spectrum provides direct molecular evidence for ammonia formation during NORR over CVS. The characteristic triplet peaks between 6.8 and 7.2 ppm correspond to the ammonium ion (NH_4^+), while the sharp signal at ~6.3 ppm arises from maleic acid, employed as an internal standard. The clear resolution and strong intensity of NH_4^+ signals, without interference from other nitrogenous byproducts, confirm the high selectivity of CVS toward ammonia production (Figures S13 and S14 and Figure 6c). The detailed experimental procedure for ^{1}H-NMR analysis is given in Supporting Information. In addition to this, NH_3 production in the electrolyte was also monitored and quantified using a UV–vis spectrophotometric technique based on the standard indophenol blue method Figure 6d, comparing with the optimized spectra and calibration curve (Figure S15a,b). In brief, the absorbance spectra span the wavelength range from approximately 540 to 780 nm, of the collected diluted aliquot was recorded. A prominent peak is observed around 630–660 nm,

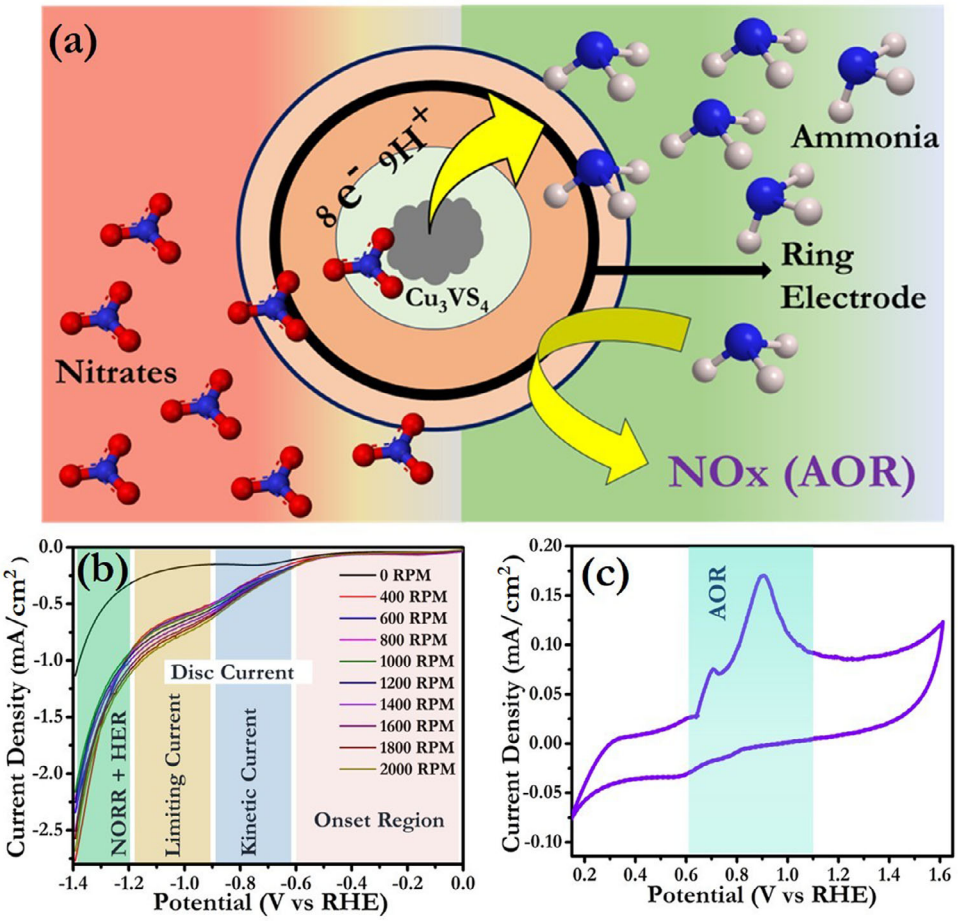

FIGURE 5 | (a) Schematic representation of RRDE (b) LSV polarization at different rotation speed at scan rate of 50 mV/sec. (c) Cyclic Voltammetry at positive potential showing the irreversible ammonia oxidation peak.

typically associated with the formation of a chromogenic product such as indophenol blue. The decreasing peak intensity across cycles indicates loss of active sites followed by a decline in the amount of ammonia produced, reflecting reduced catalytic performance over time. The other bi byproducts, like hydrazine and nitrite, were also quantified based on the calibration curve (Figures S15–S18), which shows minimal impact on overall ammonia production. The ^{1}H-NMR spectrum provides direct molecular evidence for ammonia formation during NORR over CVS. The characteristic triplet peaks between 6.8 and 7.2 ppm correspond to the ammonium ion (NH_4^+), while the sharp signal at ~6.3 ppm arises from maleic acid, employed as an internal standard. The clear resolution and strong intensity of NH_4^+ signals, without interference from other nitrogenous byproducts, confirm the high selectivity of CVS toward ammonia production, complementing the previous band energy structure findings, validating the catalyst's selective mechanistic efficiency under ambient conditions. The Faradaic efficiency obtained through spectrophotometric (Indophenol blue) analysis showed a comparable trend to the ^{1}H-NMR results, validating the accuracy and reliability of the measurements (Figure S19). The average standard deviation was calculated to be 1.19% [Table S1).

Further, driven by the high nitrate reduction activity of the catalyst and to confirm its selective conversion pathway toward ammonia over hydrogen under negative bias, electrocatalytic experiments were performed in a custom-designed gas-tight H-type cell with two compartments separated by a Nafion 117 membrane. This configuration enabled selective ionic transfer while preventing gas crossover. Each compartment was filled with a mixed electrolyte containing 0.1 M K_2SO_4 and 0.5 M KNO_3, and chronoamperometry was conducted at controlled potentials. (The detailed Experimental setup was described in the supporting information) At an applied potential of −0.9 V versus RHE, the Gas Chromatography (GC) result exhibited a strong ammonia peak at ~1.6 min, representing ~71.6% of the detected products, along with a smaller hydrogen peak (~25.3%) at ~16 min (Figure 6e). This indicates that under mild cathodic bias, nitrate reduction predominantly yields ammonia with suppressed hydrogen evolution. In contrast, at −1.4 V versus RHE, the selectivity shifted dramatically: hydrogen became the major product (~89.6%), while ammonia production decreased sharply to ~5.6% (Figure 6f). These results clearly reveal the potential-dependent competition between NORR and the HER, where excessive cathodic bias favors H_2 generation over ammonia selectivity, which is an outstanding advantage for the as-designed electrocatalyst, as it shows significantly lower overpotential for NORR over HER. Further, the distinct product peaks and quantitative yields underscore the efficiency of the catalytic system at moderate potential and the robustness of the GC analysis.

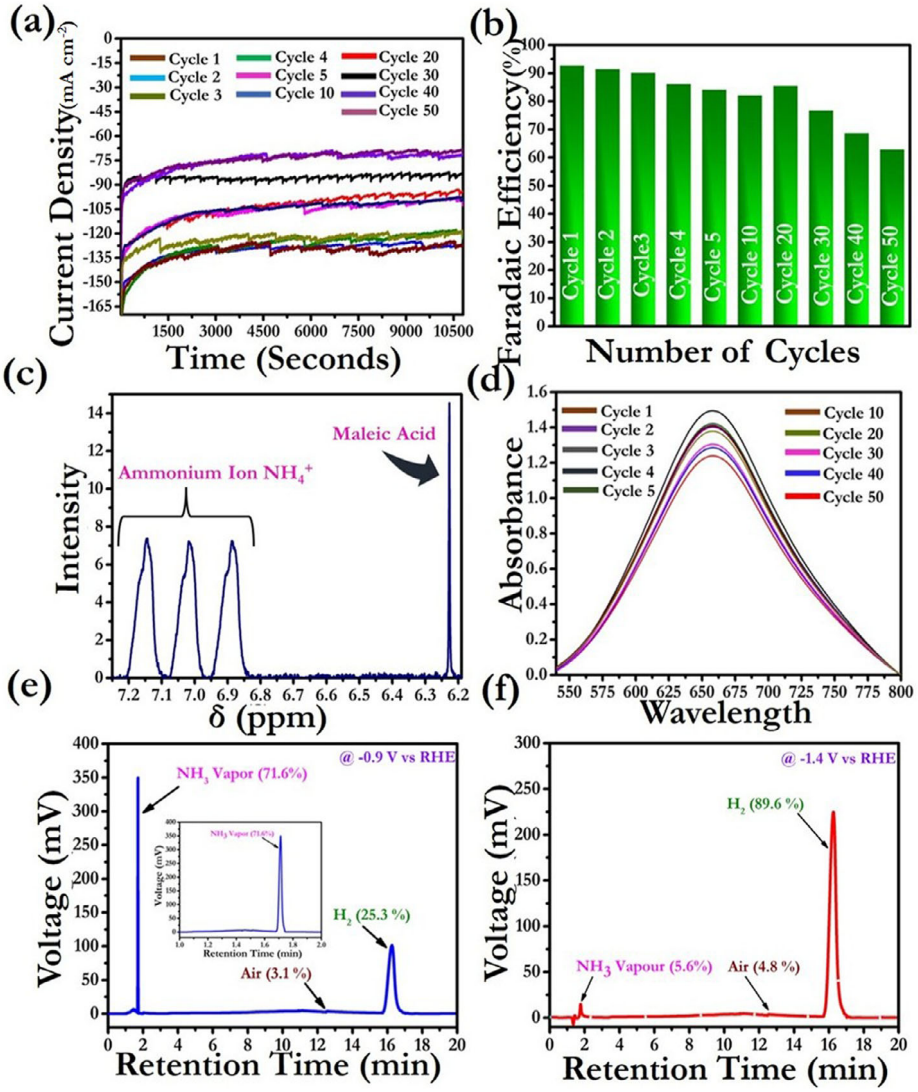

FIGURE 6 | (a) CA measurement at −1.3 V versus RHE for 50 consecutive cycles (b) the FE (%) over several catalytic Cycles corresponding UV–vis spectra for NH_3 detection through the indophenol blue method (c) ^{1}H-NMR spectrum of the aliquot obtained from the chronoamperometric experiment of the CVS catalyst at −1.3 V versus RHE (d) UV–vis spectra for NH_3 detection through the indophenol blue method at different catalytic cycle (e) Gas chromatograms of NORR products collected at applied potentials of (e) −0.9 V and (f) −1.4 V versus RHE. The inset in (e) shows the GC signal corresponding to ammonia vapor.

Together, these findings highlight that with this kind of active catalyst, the near-neutral electrolyte system (pH ~7) enables effective nitrate-to-ammonia conversion at lower overpotentials, while HER dominates at higher cathodic bias, underscoring the importance of optimizing applied potential and designing robust electrocatalysts to maximize ammonia selectivity. Comprehensive experimental details regarding the quantification of products and by-products are described in the Section S3. To augment this observation, ex situ FTIR analysis has also been performed on the collected reaction electrolyte at defined time intervals. The characteristic vibrational features [Table S2) associated with surface-bound nitrogen species provide additional evidence for the formation and evolution of key intermediates, thereby supporting a PCET mechanism governing the nitrate-to-ammonia conversion (Figure S20).

After obtaining the CA performances, it is necessary to evaluate the interfacial charge transfer processes through electrochemical impedance spectroscopy (EIS) by varying input potentials. The Nyquist plots of CVS were (Figure S21a) recorded at −1.2, −1.3, and −1.4 V versus RHE. The impedance spectra are characterized by depressed semicircles followed by diffusion-related tails, indicating a combination of charge transfer resistance and mass transport limitations. (Figure S21b–d) shows the equivalent circuit used to model the system, consisting of a series resistance indicating the solution resistance (R_s), a parallel resistance (R_{ct}) representing the charge transfer resistance, a Warburg component (W) and a constant phase element (CPE) that accounts for surface heterogeneity and non-ideal double-layer capacitance. The EIS plots for VS_2 and CuS are depicted in (Figure S22) in the same electrolyte medium varying similar potentials, and the results are depicted in Table S3. The results clearly indicate that the CVS catalyst shows much higher charge transfer efficiency *w.r.t.* the VS_2 and CuS catalysts. The value of all the crucial EIS parameters again confirms the Cu-V synergy, which is beneficial for efficient charge transfer kinetics through the moderately

TABLE 1 | Comparison of EIS parameters of all the catalyst at −1.3 V vs RHE.

Catalyst	R_s (Ohm)	R_{ct} (Ohm)	CPE
CVS	9.98	2.17	14.6 μMho*sˆN N = 0.631
VS_2	15.2	3.86	8.65 μMho*sˆN N = 0.597
CuS	11.4	3.83	10.6 μMho*sˆN N = 0.303

rough/porous electrode surface for CVS compared to other binary counterparts. The EIS parameters recorded at −1.3 V is shown in Table 1.

The relatively low R_{ct} of 2.17 Ω (@−1.3 V) observed for CVS can be attributed to its unique crystal structure and electronic configuration, where a narrow bandgap (~1.7–1.9 eV) and significant d-d orbital overlap between Cu and V centers, enhancing its electrical conductivity. Additionally, the presence of sulfur supports faster electron mobility and favorable adsorption of redox-active species at the surface. The value of the CPE exponent (N = 0.642) reflects the intrinsic surface roughness and moderate microstructural inhomogeneity, typical of sulvanite-type materials can be well-connected, with good electrolyte penetration and fast charge transfer. These structural features synergistically contribute to effective charge transport, making CVS a promising candidate for potential electrocatalytic nitrate reduction. It has been encountered that the as-designed ternary sulfide demonstrates the lowest Rct and the 'N' value above 0.5, indicating intrinsic crystal imperfections. This supports the idea that CVS can provide enhanced electroactive surface area and complex interfacial dynamics that are beneficial for electrocatalytic applications. On contrary the individual components CuS and VS_2 show the higher Rct value and the 'N' value less than 0.5, indicating (i) possibly non-uniform current distribution or poorly connected interfaces (ii) varied electronic environments within the material, (iii) weak interaction between electrolyte ions and electrode surface, (iv) rapid dissolution or corrosion processes, (v) surface passivation or fouling during measurement and (vi) electrochemical aging or degradation during prolonged testing. Besides these the ECSA plays a pivotal role in governing the electrocatalytic performance of materials for the NORR. A higher ECSA indicates more electrochemically accessible active sites, which can significantly enhance the adsorption and activation of nitrogenous molecules, leading to improved reaction kinetics and overall catalytic efficiency. To calculate the ECSA of each of the catalysts deposited on the electrode surface, cyclic voltammetry (CV) was performed for each of the catalysts within a non-faradaic potential window, varying the scan rate. The CV plots for CVS were recorded at various scan rates ranging from 20 to 140 mV/sec, and the Δj (difference in current density at a fixed potential) shows a linear relationship with scan rate, yielding a C_{dl} of 23.97 mF cm^{-2} (calculated using Equation S5). This high value suggests a large ECSA, which is obtained to be 299.62 cm^2 (Equation S6). However, with respect to the CVS, the VS_2 and the CuS exhibit significantly lower C_{dl} values (15.3 and 4.52 mF cm^{-2}), giving rise to reportedly low ECSA (191.25 and 56.5 cm^2) (Figure S23a–f). This observation supports the enhanced charge transportation and potential for electrocatalytic activity of CVS. Furthermore, a higher roughness factor (RF) indicates more exposed active sites per unit area, enhancing electrolyte accessibility (calculated using Equation S7), facilitating reactant adsorption and electron transfer, leading to higher current densities. The corresponding values are CVS shows the highest RF of 599.24, suggesting a larger number of active sites compared to VS_2 (382.5) and CuS (113).

To confirm the post-electrocatalytic stability, PXRD and TEM analyses were performed, which revealed minor changes in both phase and morphology even after extended catalytic investigations (Figure S24). Future efforts may focus on developing more robust catalyst structures, protective coatings, or regeneration strategies to sustain high performance over extended cycling. These characteristics collectively suggest that CVS possesses a superior electrocatalytic interface for facilitating NORR, which would likely result in significant ammonia yield and notable FE under identical experimental conditions.

To gain atomic-level insight into the reaction kinetics, charge density was theoretically calculated upon nitrate adsorption onto the catalyst's surface (Figure 7a,b). In this regard, Figures S25–S27 shows the charge accumulation and depletion regions, highlighting the nature of interaction between the nitrate ion and the catalyst surface, providing insights into the adsorption mechanism and electronic structure modulation. The calculated binding energy of NO_3^- on the CVS surface is approximately −0.515 eV, indicating a thermodynamically favorable and moderately strong interaction with the catalyst. In comparison, the adsorption energies of NO_3^- on CuS and VS_2 were found to be significantly higher, at 3.34 and 3.63 eV, respectively, suggesting that these surfaces are less favorable for NO_3^- adsorption. This preferential adsorption is likely a key factor contributing to the enhanced electrocatalytic performance of CVS. The probable explanation for this kind of observation can be supported by the previous electronic structure studies of CVS nanocrystals by Dong et al. [45]. They have found an intermediate band, predominantly composed of V 3d states, situated between the valence and conduction bands, which creates distinct coordination environments at the metal centers. Importantly, XPS further showed that vanadium is present in mixed oxidation states, 54.9% V^{4+} and 45.1% $V^{5+,}$ while copper exists mainly as Cu^+ (84.8%) with a minor Cu^{2+} fraction (15.2%). The NO_3^- ion behaves as a hard base owing to the low polarizability of its small oxygen donor atoms, rendering it a weak Lewis base and a relatively poor ligand. Whereas, in CVS, the V^{4+}/V^{5+} centers behave as hard acids by virtue of their high oxidation states, high charge densities, and small ionic radii, whereas the Cu^+/Cu^{2+} centers are softer acids, characterized by lower oxidation states, lower charge densities, and larger ionic radii. According to Hard-Soft Acid-Base (HSAB) theory, hard acids preferentially bind to hard bases; along with the higher oxidation states of vanadium confer a stronger electrostatic attraction for the nitrate ion compared to copper. In this view, the two charge density difference plots in this work provide complementary perspectives on the nitrate binding interaction on the V-Cu surface. In the first image (side view) shown in Figure 7a, the nitrate is clearly adsorbed above a vanadium (V, red) site, with substantial charge depletion (cyan) observed around the V atom. In contrast, the surrounding copper (Cu, blue & S, green) atoms show negligible charge redistribution, suggesting their limited involvement in the binding interaction. The second image

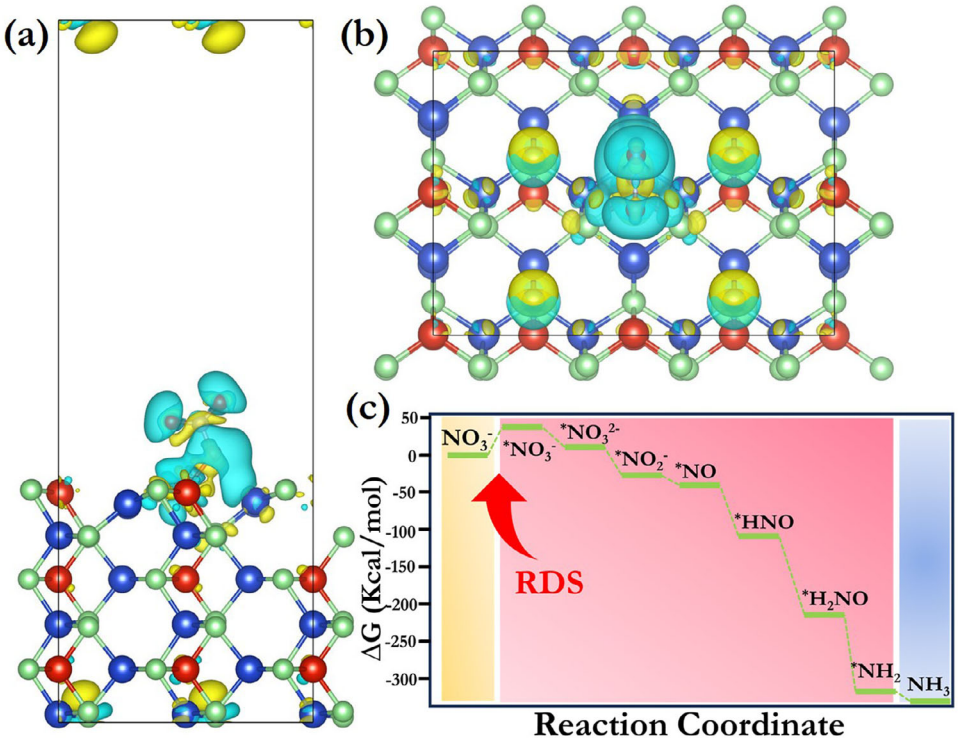

FIGURE 7 | (a) Top and (b) side views of charge density difference for NO_3^- adsorbed over CVS surface. The yellow and blue regions represent electron accumulation and depletion, respectively, with an isosurface value of 0.0003 e/Å^3. (c) Gibbs free energy profile for the electrocatalytic NORR to NH_3 over CVS slab model corresponding to (110) plane.

(top view) shown in Figure 7b reinforces this observation by highlighting strong charge accumulation and depletion directly over the central V atom. The symmetrical lobes above the vanadium further suggest notable orbital overlap between V and nitrate, consistent with covalent or coordinate bonding. Meanwhile, the Cu atoms exhibit minimal electronic rearrangement, reinforcing their secondary role. Together, these plots provide clear evidence that nitrate preferentially binds to the vanadium site, establishing V as the primary active center in the bimetallic system, which is again supported by the XPS data, where we get V^{5+} oxidation states. Figure 7c and Table S4 represent the Gibbs free energy profile for the electrocatalytic NORR to NH_3 over CVS, highlighting the stepwise transformation of surface-bound intermediates through PCET mechanisms. The process begins with NO_3^- adsorption on the catalyst surface ($*NO_3^-$) followed by stepwise reduction through intermediates such as $*NO_2^-$, *NO, *HNO, and $*H_2NO$. The initial step, adsorption and activation of NO_3^- to form $*NO_3^-$ emerges as the rate-determining step (RDS), due to its significant uphill free energy of +34.337 kcal/mol, indicating the highest energy barrier along the reaction coordinate. Subsequent reductions are exergonic, especially the transformation from *NO to *HNO, indicating favorable energetics. The final steps to $*NH_2$ and NH_3 are highly downhill, reflecting the strong thermodynamic driving force for NH_3 formation. This energy landscape highlights the importance of catalyst design in stabilizing intermediates and lowering kinetic barriers to enhance both activity and selectivity in NORR. When adsorption is rate-limiting, the nature of the active sites, their electronic structure, oxidation state, and orbital hybridization capabilities become critical. In the case of oxo-anions like NO_3^-, the catalyst must provide oxophilic centers (like V) to bind and activate NO_3^- through strong V-O interactions, making it easier to inject electrons into the π^* orbitals of NO_3^-. These insights underscore the synergistic catalytic function of CVS, where V facilitates nitrate adsorption followed by efficient charge transport supported by Cu, together enabling favorable NORR kinetics and selectivity toward green NH_3 production. The Gibbs free energy values calculated for the formation of all intermediates during the NORR process over the CVS catalyst are summarized in Section S5 and Table S2. The detailed computational measurement protocols have been depicted in Section S4.

As a practical viability, real-time electrocatalysis was conducted on agricultural runoff water collected from Odisha University of Agriculture and Technology (OUAT), Bhubaneswar, Odisha, India. Initially, the collected water sample was centrifuged and filtered to remove suspended particulates and soil residues (Figure 8a). The nitrate concentration in the filtered water was then quantified using a spectrophotometer. The pH of the solution was adjusted to neutral before electrochemical reduction studies, and the LSV was performed at a scan rate of 10 mV s^{-1} (Figure 8b). The steady-state current density at an applied potential of −0.79 V was observed to be approximately −36 mA cm^{-2}. It is noteworthy that this current density was slightly lower than that observed in previous controlled experiments, possibly due to the interference of other ionic or organic impurities present in the real sample. Subsequently, CA measurements were carried out for 30 min over two consecutive cycles to evaluate the catalytic performance (Figure 8c). Post-reaction, the nitrate concentration was re-measured spectrophotometrically, revealing a conversion efficiency of approximately 59%,

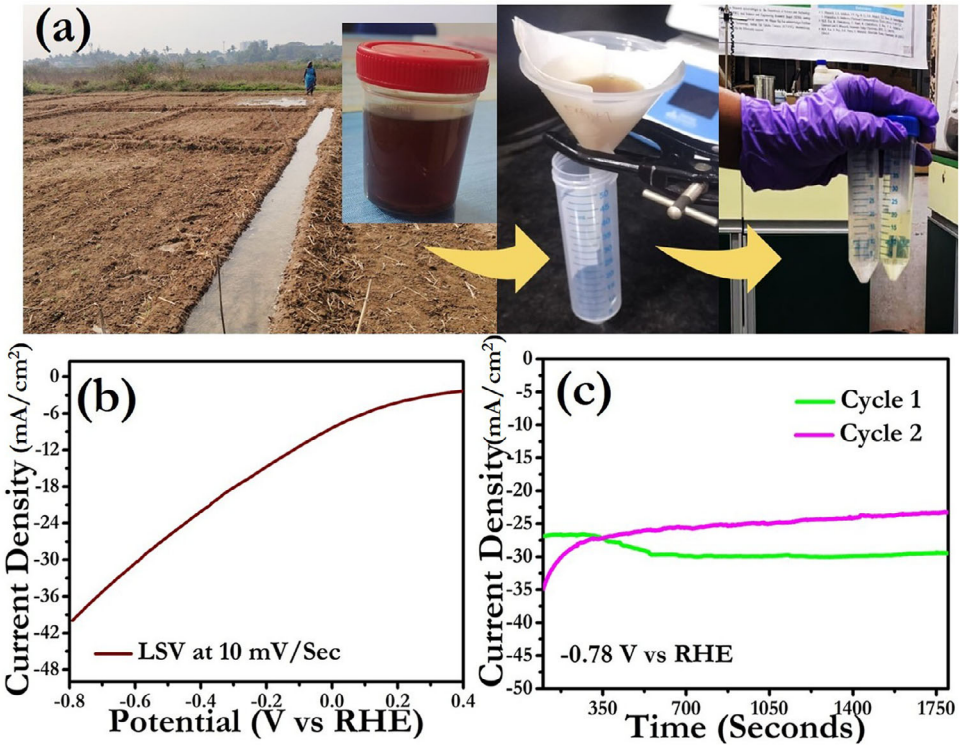

FIGURE 8 | (a) Agricultural runoff water was collected from the vicinity of a nearby agricultural university for experimental analysis (b) LSV polarization curve using CVS as a catalyst at a scan rate of 10 mv/sec (c) Chronoamperometric curve for subsequent two cycles at applied potential of −0.78 V versus RHE.

thereby confirming the ready-to-use practicability of the catalyst under real environmental conditions. A complete literature comparison of crucial parameters related to NH_3 production and real-world performance with our material is consolidated in Table S5, which shows the as-designed CVS has tremendous future implications toward green energy application upon further modification.

3 | Conclusion

In this study, the idea of a novel ternary Cu-V-S (CVS) nanoelectrocatalyst was conceived and successfully developed as a strong potential candidate for efficient electrocatalysis toward nitrate remediation and green ammonia synthesis. To the best of our current knowledge, this catalyst has not been explored previously, representing a new class of material with promising catalytic prospects for various electrochemical as well as photochemical applications. The optimized electronic structure, ideal band energy alignment, and well-engineered surface architecture collectively enable favorable reaction thermodynamics and superior charge transfer kinetics. As a result, the material exhibits outstanding electrocatalytic performance, with a significantly low onset and overpotentials of −0.476 and −0.596 V at 10 mA cm^{-2}, with notably faster charge transfer kinetics having a Tafel slope value of 34.1 mV dec^{-1} compared to benchmark catalysts. Further, the high ECSA of 299.62 cm^2 and roughness factor of 599.24 support enhanced nitrate adsorption followed by facile reduction to ammonia, contributing to its superior catalytic behavior. Another important parameter of the catalyst, specifically its stability, was evaluated over multiple catalytic cycles (up to the 50th cycle). The catalyst exhibited a notably high FE of 91% and an ammonia yield of 79 000 μg h^{-1} mg^{-1}, maintaining both consistently over long repeated cycles. Moreover, the catalyst also demonstrates selectivity toward green ammonia production over hydrogen with distinguished input potentials, examined by systematic integration of GC experiments. The extensive theoretical study confirms the experimental observations by evaluating reaction energetics, including the RDS across the intermediates, which clearly demonstrate the strong synergistic interaction between V and Cu, further highlighting the applicability of this catalyst as an efficient electroactive material. Finally, real-world application tests using agricultural runoff water further enforce the catalyst's technological relevance not only for environmental pollution mitigation but also for significant ammonia production with a conversion rate of 59%. Overall, this newly designed CVS nanocrystals present a catalytically promising, stable, and eco-friendly solution for efficient electrochemical green ammonia production strategy, offering valuable prospects for sustainable nitrogen management and industrially relevant green energy applications.

Author Contributions

N.M. conceptualized the study and provided overall supervision. S.S. and J.S. performed all the experiments, designed the Methodology, wrote the original manuscript and equally contributed. DFT calculations and analyses were carried out by R.S. and A.M. U.T., and S.C. helped in performing the experiment and Data interpretation. S.M. helped in analysis. All authors reviewed the writing of the manuscript based on their respective areas of expertise.

Acknowledgements

The authors sincerely acknowledge the Institute of Chemical Technology Mumbai-Indian Oil Odisha Campus, Bhubaneswar, Energy and Environmental Laboratory, Department of Chemistry, Institute of Science, Banaras Hindu University, Varanasi, UP-221005, India. Department of Chemistry, Institute of Science, Banaras Hindu University, Varanasi, UP-221005, India. Indian Institute of Technology Gandhinagar, Palaj, Gandhinagar, Gujarat, and UGC-DAE Consortium for Scientific Research, University Campus, Khandwa Road, Indore, for providing instrumental facilities and support. The authors are grateful to Akanksha Baliarsingh, Project Assistant, Department of Soil Science and Agricultural Chemistry, CA, OUAT (OUAT), for providing agricultural run-off water for the experiment. Additionally, this research was also supported by the UGC-DAE-CSR grant (CRS/2021-22/01/365), Core Research Grant (CRG/2022/005380), and National Postdoctoral Fellowship (PDF/2023/000211).

Conflicts of Interest

The authors declare no conflicts of interest.

Data Availability Statement

The data that support the findings of this study are available from the corresponding author upon reasonable request.

References

1. S. M. Garvey, E. A. Davidson, C. Wagner-Riddle, et al., "Emerging Opportunities and Research Questions for Green Ammonia Adoption in Agriculture and Beyond," *Nature Reviews Clean Technology* 1 (2025): 10–11.

2. S. Fahimirad, M. Memarzadeh, H. Jafari, M. S. Isfahani, A. Almasi-Hashiani, and H. Abtahi, "Enhanced Wound Healing and Antibacterial Efficacy of a Novel Chitosan Quaternary Ammonium Salt Gel Incorporating Echinacea purpurea Extract," *Carbohydrate Research* 552 (2025): 109445, https://doi.org/10.1016/j.carres.2025.109445.

3. H. Guo, Y. Zhou, K. Chu, et al., "Improved Ammonia Synthesis and Energy Output from Zinc-Nitrate Batteries by Spin-State Regulation in Perovskite Oxides," *Journal of the American Chemical Society* 147 (2025): 3119–3128, https://doi.org/10.1021/jacs.4c12240.

4. J. L. Tiggeloven, A. P. C. Faaij, G. J. Kramer, and M. Gazzani, "Optimizing Emissions Reduction in Ammonia–Ethylene Chemical Clusters: Synergistic Integration of Electrification, Carbon Capture, and Hydrogen," *Industrial & Engineering Chemistry Research* 64 (2025): 4479–4497, https://doi.org/10.1021/acs.iecr.4c03817.

5. S. Li, Q. Zhao, J. Xiong, et al., "Influence of Water on Liquid Ammonia-Based Sustainable Dyeing of Ramie fiber," *Arabian Journal of Chemistry* 18 (2025): 106043, https://doi.org/10.1016/j.arabjc.2024.106043.

6. Y. Hu and Z. Tan, "Enhanced Ammonia-sensitive Intelligent Films Based on a Metal-Organic Framework for Accurate Shrimp Freshness Monitoring," *Food Chemistry* 471 (2025): 142805, https://doi.org/10.1016/j.foodchem.2025.142805.

7. L. D. Elliott, "The Molecular Lowering of the Freezing Point of Liquid Ammonia," *The Journal of Physical Chemistry* 28 (1924): 611–635, https://doi.org/10.1021/j150240a005.

8. W. Tang, X. Xu, Y. Cheng, et al., "The Interfacial Association Dehydrogenation Mechanism Guides the Design of Anode Pt-Based Catalysts for Direct Ammonia Fuel Cells: a Perspective," *Chemical Engineering Journal* 510 (2025): 161867, https://doi.org/10.1016/j.cej.2025.161867.

9. J. Han, M. Wen, Y. Hong, et al., "Theoretical Research on the Combustion Characteristics of Ammonium Dinitramide-Based Non-Toxic Aerospace Propellant," *Aerospace* 12 (2025): 295, https://doi.org/10.3390/aerospace12040295.

10. F. Haber and R. L. Rossignol, "The Production of Synthetic Ammonia," *Journal of Industrial & Engineering Chemistry* 5 (1913): 328–331, https://doi.org/10.1021/ie50052a022.

11. V. Kyriakou, I. Garagounis, A. Vourros, E. Vasileiou, and M. Stoukides, "An Electrochemical Haber-Bosch Process," *Joule* 4 (2020): 142–158, https://doi.org/10.1016/j.joule.2019.10.006.

12. Z. Wang, Z. Yang, K. Otake, et al., "Metal-Organic Frameworks for Advanced Electrochemical Ammonia Production in Water," *ChemElectroChem* 12 (2025): 202400525, https://doi.org/10.1002/celc.202400525.

13. M. Moosazadeh, A. Mansourimarand, S. Ajori, V. Taghikhani, and C. Yoo, "Waste-to-Ammonia: a Sustainable Pathway for Energy Transition," *Renewable and Sustainable Energy Reviews* 208 (2025): 115012, https://doi.org/10.1016/j.rser.2024.115012.

14. T. Tang, B. Li, M. Lu, Y. Feng, and J. Wang, "Synergistic Geothermal Energy and Ammonia Fuel Cell Utilization towards Sustainable Power, Cooling, and Freshwater Production; an Exergoeconomic, Exergoenvironmental, and Technoeconomic Analysis," *Renewable Energy* 241 (2025): 122244, https://doi.org/10.1016/j.renene.2024.122244.

15. S. Ingavale, P. Marbaniang, M. Palabathuni, and N. Mishra, "In Situ Growth of Copper Oxide on MXene by Combustion Method for Electrochemical Ammonia Production from Nitrate," *Nanoscale Advances* 6 (2024): 481–488, https://doi.org/10.1039/D3NA00609C.

16. K. Chu, B. Weng, Z. Lu, et al., "Exploration of Multidimensional Structural Optimization and Regulation Mechanisms: Catalysts and Reaction Environments in Electrochemical Ammonia Synthesis," *Advanced Science* 12 (2025): 2416053, https://doi.org/10.1002/advs.202416053.

17. S. M. Gowdru, P. H. Nagaraju, Y.-C. Chen, K.-C. Wu, C.-C. Chang, and D.-Y. Wang, "Enhanced Electrocatalytic Nitrate Reduction to Ammonia on Silver Nanocubes," *Chemical Communications* 61 (2025): 6965–6968, https://doi.org/10.1039/D5CC01409C.

18. S. Ingavale, P. Marbaniang, M. Palabathuni, V. N. Kale, and N. Mishra, "Decoration of Boron Nanoparticles on a Graphene Sheet for Ammonia Production from Nitrate," *Nanoscale* 15 (2023): 11497–11505, https://doi.org/10.1039/D3NR01089A.

19. H. Zhang, H. Wang, X. Cao, et al., "Unveiling Cutting-Edge Developments in Electrocatalytic Nitrate-to-Ammonia Conversion," *Advanced Materials* 36 (2024): 2312746, https://doi.org/10.1002/adma.202312746.

20. H. Lin, J. Wei, Y. Guo, et al., "Bi_1 -$CuCo_2$ O_4 Hollow Carbon Nanofibers Boosts NH_3 Production from Electrocatalytic Nitrate Reduction," *Advanced Functional Materials* 34 (2024): 2409696, https://doi.org/10.1002/adfm.202409696.

21. J. Wei, G. Ye, H. Lin, Z. Li, J. Zhou, and Y. Li, "Enhanced Electrochemical Nitrate Reduction on Copper Nitride with Moderate Intermediates Adsorption," *Journal of Colloid and Interface Science* 670 (2024): 798–807, https://doi.org/10.1016/j.jcis.2024.05.084.

22. J. Huang, Z. Qu, Y. Gao, et al., "Sustainable Liquid Nitrogen Fertilizer Production via Air Plasma Bubbles: Insights into Plasma-Enabled N_2 Fixation Chemistry," *Journal of Physics D: Applied Physics* 58 (2025): 115207, https://doi.org/10.1088/1361-6463/ada6c7.

23. Y. Tang, X. Ma, Y. Zhao, et al., "Manure Application Rather than Plastic-film Uncovering to Sustainably Alleviate Plastic-greenhouse Soil Nitrate Surplus and Salinity in Yangtze River Delta," *Agricultural Water Management* 312 (2025): 109437, https://doi.org/10.1016/j.agwat.2025.109437.

24. M. Schaenen, Q. Tang, J. Li, and M. Hassani, "Chemical Strengthening of Glass Powder Particles," *Scripta Materialia* 255 (2025): 116368, https://doi.org/10.1016/j.scriptamat.2024.116368.

25. A. M. Djerdjev, P. Priyananda, P. Fitzgerald, et al., "Surfactant Induced Crystallisation of Emulsion Explosives via Spinodal Decomposition," *Journal of Molecular Liquids* 424 (2025): 127146, https://doi.org/10.1016/j.molliq.2025.127146.

26. E. Britt, H. A. López Peña, J. M. Shusterman, K. Sangroula, K. U. Lao, and K. M. Tibbetts, "Ultrafast Dissociation Dynamics of the Sensitive Explosive Ethylene Glycol Dinitrate," *The Journal of Physical Chemistry Letters* 16 (2025): 882–888, https://doi.org/10.1021/acs.jpclett.4c03220.

27. J. Zeng, Z. Gu, J. Li, et al., "Nitrate Supply Increases the Resistance of Cucumber to Fusarium Wilt Disease by Regulating Root Exudation,"

Biology and Fertility of Soils 61 (2025): 805–820, https://doi.org/10.1007/s00374-025-01895-4.

28. L. Ma, L. Hu, X. Feng, and S. Wang, "Nitrate and Nitrite in Health and Disease," *Aging and Disease* 9 (2018): 938–945, https://doi.org/10.14336/AD.2017.1207.

29. P. H. van Langevelde, I. Katsounaros, and M. T. M. Koper, "Electrocatalytic Nitrate Reduction for Sustainable Ammonia Production," *Joule* 5 (2021): 290–294, https://doi.org/10.1016/j.joule.2020.12.025.

30. D. Liu, L. Qiao, S. Peng, et al., "Recent Advances in Electrocatalysts for Efficient Nitrate Reduction to Ammonia," *Advanced Functional Materials* 33 (2023): 2303480, https://doi.org/10.1002/adfm.202303480.

31. D. Zhu, M. Qiao, J. Liu, T. Tao, and C. Guo, "Engineering Pristine 2D Metal–organic Framework Nanosheets for Electrocatalysis," *Journal of Materials Chemistry A* 8 (2020): 8143–8170, https://doi.org/10.1039/D0TA03138K.

32. A. Arulraj, P. K. Murugesan, F. V. Herrera, and R. V. Mangalaraja, "Rational Designing of Ternary CuSSe Electrocatalyst for Water Splitting: Layered Mastery of 2D Nanostructures," *International Journal of Hydrogen Energy* 104 (2025): 313–323, https://doi.org/10.1016/j.ijhydene.2024.06.184.

33. B. Bai, Y. Wan, W. Yan, and J. Zhang, "2D materials Design and Property Modulation for Electrocatalytic Nitrate Reduction to Ammonia," *2D Materials* 12 (2025): 022006, https://doi.org/10.1088/2053-1583/adb43e.

34. H. Begum, M. D. N. Islam, S. Ben Aoun, et al., "Electrocatalytic Reduction of Nitrate Ions in Neutral Medium at Coinage Metal-modified Platinum Electrodes," *Environmental Science and Pollution Research* 30 (2022): 34904–34914, https://doi.org/10.1007/s11356-022-24372-z.

35. K. Zhang, Y. Liu, Z. Pan, et al., "Cu-based Catalysts for Electrocatalytic Nitrate Reduction to Ammonia: Fundamentals and Recent Advances," *EES Catalysis* 2 (2024): 727–752, https://doi.org/10.1039/D4EY00002A.

36. Y. Wang, W. Zhou, R. Jia, Y. Yu, and B. Zhang, "Unveiling the Activity Origin of a Copper-Based Electrocatalyst for Selective Nitrate Reduction to Ammonia," *Angewandte Chemie International Edition* 59 (2020): 5350–5354, https://doi.org/10.1002/anie.201915992.

37. Y. Li, J. Wei, H. Lin, et al., "Hollow Square Ni-Doped Copper Oxide Catalyst Boosting Electrocatalytic Nitrate Reduction," *ACS Catalysis* 15 (2025): 1672–1683, https://doi.org/10.1021/acscatal.4c06705.

38. S. Popović, M. Smiljanić, P. Jovanovič, J. Vavra, R. Buonsanti, and N. Hodnik, "Stability and Degradation Mechanisms of Copper-Based Catalysts for Electrochemical CO_2 Reduction," *Angewandte Chemie International Edition* 59 (2020): 14736–14854.

39. J. Zhao, L. Liu, Y. Yang, et al., "Insights into Electrocatalytic Nitrate Reduction to Ammonia via Cu-Based Bimetallic Catalysts," *ACS Sustainable Chemistry & Engineering* 11 (2023): 2468–2475, https://doi.org/10.1021/acssuschemeng.2c06498.

40. G. A. Cerrón-Calle, A. S. Fajardo, C. M. Sánchez-Sánchez, and S. Garcia-Segura, "Highly Reactive Cu-Pt Bimetallic 3D-electrocatalyst for Selective Nitrate Reduction to Ammonia," *Applied Catalysis B: Environmental* 302 (2022): 120844, https://doi.org/10.1016/j.apcatb.2021.120844.

41. Y. Zhou, R. Duan, H. Li, M. Zhao, C. Ding, and C. Li, "Boosting Electrocatalytic Nitrate Reduction to Ammonia via Promoting Water Dissociation," *ACS Catalysis* 13 (2023): 10846–10854, https://doi.org/10.1021/acscatal.3c02951.

42. A. Giri, G. Park, and U. Jeong, "Layer-Structured Anisotropic Metal Chalcogenides: Recent Advances in Synthesis, Modulation, and Applications," *Chemical Reviews* 123 (2023): 3329–3442, https://doi.org/10.1021/acs.chemrev.2c00455.

43. J. Choi, H. Lim, S. Surendran, et al., "Dichalcogenides as Emerging Electrocatalysts for Efficient Ammonia Synthesis: a Focus on Mechanisms and Theoretical Potentials," *Advanced Functional Materials* 35 (2025): 2422585, https://doi.org/10.1002/adfm.202422585.

44. W. J. Albery, G. J. O'Shea, and A. L. Smith, "Interpretation and Use of Mott–Schottky Plots at the Semiconductor/Electrolyte Interface," *Journal of the Chemical Society, Faraday Transactions* 92 (1996): 4083–4085, https://doi.org/10.1039/FT9969204083.

45. Y. Dong, S. Dong, C. Yu, et al., "Mitochondria-Targeting Cu_3VS_4 Nanostructure with High Copper Ionic Mobility for Photothermoelectric Therapy," *Science Advances* 9 (2023): 1.

46. B. Pejjai, M. Reddivari, and T. R. R. Kotte, "Phase Controllable Synthesis of CuS Nanoparticles by Chemical co-precipitation Method: Effect of Copper Precursors on the Properties of CuS," *Materials Chemistry and Physics* 239 (2020): 122030, https://doi.org/10.1016/j.matchemphys.2019.122030.

47. S. A. Patil, I. Rabani, S. Hussain, et al., "A Facile Design of Solution-Phase Based VS_2 Multifunctional Electrode for Green Energy Harvesting and Storage," *Nanomaterials* 12 (2022): 339, https://doi.org/10.3390/nano12030339.

48. Y.-H. Liu, P.-W. Huang, and M. C. Hatzell, "A Rotating Ring Disc Electrode Study of Photo(electro)Catalyst for Nitrogen Fixation," *Faraday Discussions* 243 (2023): 378–387, https://doi.org/10.1039/D2FD00168C.

Supporting Information

Additional supporting information can be found online in the Supporting Information section.

Supporting File: smll72300-sup-0001-SuppMat.docx